# Measurement of the differential cross section of the photoinitiated reactive collision of O($^1$D)+D$_2$ using only one molecular beam: A study by three dimensional velocity mapping

S. Kauczok,[1,a)] C. Maul,[1] A. I. Chichinin,[2] and K.-H. Gericke[1]

[1]*Institut für Physikalische und Theoretische Chemie, TU Braunschweig, 38106 Braunschweig, Germany*
[2]*Institute of Chemical Kinetics and Combustion, 630090 Novosibirsk, Russia*

In order to measure the state selective double differential cross section of a reactive collision, the preparation of the reactants with defined initial velocities and quantum states in number densities high enough to achieve an acceptable count rate is most important. At the same time, secondary collisions have to be prevented in order to ensure that the nascent products are not thermalized. Usually, the best way to control the initial conditions is to use crossed molecular beams, but the number density decreases quadratically with the distance from the nozzle orifice which can be a problem, especially if a molecular product with a large number of populated states is to be analyzed state specifically by REMPI spectroscopy. In this contribution we would like to present a method for measuring the quantum state selective differential cross section of a photoinitiated reaction that combines the advantages of the PHOTOLOC technique (high reactant densities) and the parallel beams technique used by the groups of Kitsopoulos, Orr-Ewing, and Suits (defined relative velocity of the reactants). Moreover, an algorithm based on a Bayesian backward reconstruction developed by W. H. Richardson [J. Opt. Soc. Am. **62**, 55 (1972)] has been derived. Both, one reactant and the precursor of the other reactant, are present in the same molecular beam and the center of mass velocity is selected by shifting the dissociation and the detection laser in time and space. Like in comparable methods, this produces a bias in the measured velocity distribution due to the fact that the reaction takes place in the whole volume surrounding the laser beams. This has been also reported by Toomes *et al.* in the case of the parallel beams technique and presents a general problem of probing reaction products by REMPI spectroscopy. To account for this, we develop a general approach that can be easily adapted to other conditions. The bias is removed in addition to deconvolution from the spread in reactant velocities. Using the benchmark system O($^1$D)+D$_2$ with N$_2$O as the precursor, we demonstrate that the technique is also applicable in a very general sense (i.e., also with a large spread in reactant velocities, products much faster than reactants) and therefore can be used also if such unfortunate conditions cannot be avoided. Since the resulting distribution of velocities in the laboratory frame is not cylindrically symmetric, three dimensional velocity mapping is the method of choice for the detection of the ionized products. For the reconstruction, the distance between the two laser beams is an important parameter. We have measured this distance using the photodissociation of HBr at 193 nm, detecting the H atoms near 243 nm. The collision energy resulting from the 193 nm photodissociation of N$_2$O is $5.2 \pm 1.9$ kcal/mol. Our results show a preference for backward scattered D atoms with the OH partner fragment in the high vibrational states ($v=4-6$), in accord with previously published results claiming the growing importance of a linear abstraction mechanism for collision energies higher than 2.4 kcal/mol. © *2010 American Institute of Physics.* [doi:10.1063/1.3427534]

## I. INTRODUCTION

The problem of measuring the state resolved differential cross section (DCS) of photoinitiated bimolecular reactions in one molecular beam is usually approached by using the PHOTOLOC technique[1–3] which was also further developed by Bass *et al.*[4–6] introducing a Legendre moment fitting procedure. Here, both lasers, i.e., the dissociation and analysis laser, are superimposed in time and space and thus the densities of both reactants are highest although the direction of the reactant velocity is not very well defined. The groups of Kitsopoulos, Orr-Ewing, and Suits[7–9] have developed a technique that uses two parallel molecular beams where one carries the precursor to be photolyzed and the other the target molecule. In that case, the reactant velocity is better defined, but the density is significantly lower due to the distance between the two beams. The idea behind our technique is to combine the advantages of both techniques.

We use a single molecular beam that contains both the photolysis precursor and the second reactant like in the PHOTOLOC technique, but we shift the two lasers in time and space in order to select only a small part of the three dimen-

a)Electronic mail: s.kauczok@tu-bs.de.

sional (3D) velocity distribution of the photolysis product like in the parallel beams technique. As Toomes and Kitsopoulos showed by scanning the delay between the two lasers in the case of a monoenergetic reactant speed distribution,[8] this produces some bias in the observed velocity distribution of the product due to the geometrical conditions, although Liu *et al.*[7] claimed that they were able to select reactant velocities from the broad speed distribution of the 193 nm photolysis of $SO_2$ by selecting a certain delay time. However, we found that under the conditions used here, bias in the laboratory frame product velocity distribution is present and has to be considered like in the study of Toomes *et al.*[8] (*vide infra*).

The title reaction $O(^1D) + D_2 \rightarrow OD + D$ has been studied using the $N_2O$ photolysis at 193 nm to produce the $O(^1D)$ atoms. The D atom products have been detected by REMPI[2+1]. We have made this choice in order to show the general applicability of our technique, since it could be hardly analyzed by PHOTOLOC in this way. The conditions are rather challenging because the reactant kinetic energy distribution is broad due to the internal state distribution of the $N_2$ cofragment in the $N_2O$ photolysis. Furthermore, the products are much faster than the reactants and the product speed distribution is also broad. Of course, using PHOTOLOC one would rather look at the OD cofragment state specifically, since that exhibits a monoenergetic speed distribution. It would therefore be improper to criticize PHOTOLOC here, since it has yielded fascinating and important results where applicable and the experiment design would be unreasonable if it would be used. However, we would like to stress that looking at the OD would be advantageous using our technique as well, but the purpose to choose the D atom instead is to show that the technique yields the DCS even under these unfavorable conditions. It might be easily envisaged that such conditions can be inevitable for the study of photoinitiated reactions with more complex reactants. Additionally, the reaction of $O(^1D) + D_2$ has been studied extensively in the past, so that it is an appropriate benchmark for testing the applicability of our new technique after the outcome of the analysis.

Reactions involving $O(^1D)$ are often key steps in combustion chemistry and in the photoinitiated chain reactions in atmospheric chemistry such as the reaction with water or $H_2$. These yield the important OH radical which is colloquially termed the atmosphere's detergent for its role in functionalizing nonpolar hydrocarbons with hydrophilic groups.

In particular, the reaction of $O(^1D)$ with $H_2$ and its isotopic variants (i.e., HD and $D_2$) is also of interest in fundamental reaction dynamics and has been the subject of many theoretical and experimental studies, since it behaves substantially different from reactions of halogen atoms with $H_2$ which are classical abstraction reactions.[10–25] A review article on insertion reactions of excited atoms with $H_2$ can be found in Ref. 26. Measurements of the rotational and vibrational distributions of OH showed a strongly inverted rotational distribution,[27,28] and a uniform distribution for $v'$ $= 0-3$ and a much lower population for $v' = 4$ for collision energies below 2 kcal/mol.[29–35] The rotational distribution was first interpreted to be the result of angular momentum

constraints[36–39] and the vibrational distribution does neither show the characteristics of an abstraction (inverted for an early barrier) nor a long lived intermediate (monotonically decreasing). However, more recent experimental and theoretical work showed the influence of the first two excited potential energy surfaces (PESs) $1\,^1A''$ and $2\,^1A'$ in the rovibrational distribution[40] and the reaction on the ground PES has been modeled using a statistical model for an insertion reaction.[41] The other two singlet surfaces that correlate with the ground state reactants, $2\,^1A''$ and $3\,^1A'$, could in principle also contribute to the reaction due to Coriolis coupling with the ground state PES, but their influence is thought to be negligible.[42,43] An early crossed molecular beam experiment of $O(^1D) + H_2$ with a collision energy of 2.7 kcal/mol showed forward-backward symmetry in the angular distribution indicative of an insertion mechanism forming a ground state $H_2O$ ($^1A_1$) intermediate being in a 168.1 kcal/mol (7.29 eV) deep well[44,45] with respect to the reactants. The reaction would therefore proceed solely on the lowest ($1\,^1A'$) of five PESs correlating with the products.[11] The lifetime of this intermediate does not have to be long compared to a rotational period, since the symmetry of the angular distribution can also only reflect the symmetry of the intermediate. Computations on the ground PES of $H_2O$ yielded more or less forward/backward symmetry.[46,47] However, this simple notion had to be revised, since experiments and theoretical studies showed a backward preference for certain collision energies and product states.[48,49] Measurements of the excitation function $\sigma_{rel}(E_{col})$ by Hsu *et al.* clearly showed a strong decrease up to $E_{col} \approx 2$ kcal/mol and then a slight increase with higher collision energy. This can be interpreted by an abstraction mechanism becoming important.[50] This interpretation is backed by the topology of the ground ($1\,^1A'$) and first excited state ($1\,^1A''$) PESs where the first shows no barrier at all for a $C_{2v}$ approach and the latter has a linear reaction path with a barrier of 2.4 kcal/mol.[51,52] Again, Liu *et al.* find backward scattering for $O(^1D) + HD$ for both the H and the D channel at $E_{col}$ $= 4.53$ kcal/mol,[53,54] which is qualitatively also present in the measurements at 3 kcal/mol ($H_2$) and 5.3 kcal/mol ($D_2$) of Alagia *et al.*[55] and in the velocity mapping study of $O(^1D) + D_2$ by Ahmed *et al.*[56] at 2.4 kcal/mol, but not so pronounced. Liu *et al.*[57] found that the extra backward scattered OH are in the highest vibrational levels ($v = 4-6$). An overview is also given in Ref. 58. Just recently, theoretical work on the velocity and angular momentum correlations $(k, k', J')$ has been published as well.[59,60]

In laboratory experiments, $O(^1D)$ is usually generated by photolyzing $O_3$ or $N_2O$ at 193 nm using an ArF excimer laser. Since ozone is a highly reactive gas and not easy to handle, there are situations where $N_2O$ seems to be more suitable, although the absorption cross section is not very large [$8 \times 10^{-20}$ cm$^2$ at 148 K (Ref. 61)] and decreases with lower temperatures because the excited state is bent and therefore excitation of the vibrational bending mode enhances the transition probability.[62] Other advantages for $N_2O$ are the branching ratio in strong favor of $O(^1D)$ ($>0.90$), other possible channels being more or less negligible [$O(^3P)$: (Ref. 63) $0.02 \pm 0.02$, $O(^1S)$: (Ref. 64) $<0.04$, $N(^4S)$
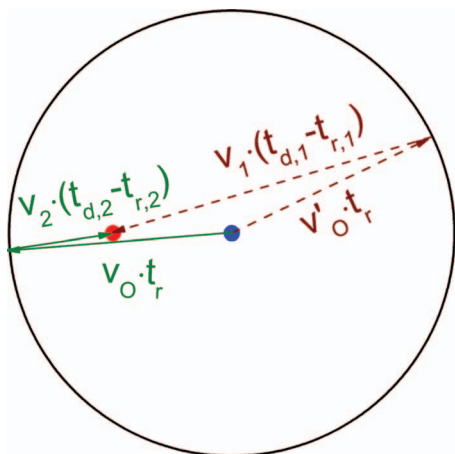
FIG. 1. Sketch showing two possible ways to detect forward scattered D atoms with the dye laser (red circle). Here the oxygen precursor is formed by the dissociation laser (blue circle) with a fixed speed and reacts at the time $t_r$. If the speed $v_1$ is large enough, the ion on path 1 (brown/dashed) can reach the detection laser and will show up in the domain of the forward scattered products.

(Ref. [65]) $(2.1 \pm 0.9) \times 10^{-3}$)] and the chemically inert partner fragment N$_2$. Both sources for O($^1$D) have in common that they are triatomic molecules which means that the excess energy of the photolysis is not only transformed into kinetic energy of the fragments ideally yielding a monoenergetic velocity distribution with an again ideally extreme $\beta$-parameter, but is also transformed into internal energy of the partner fragment resulting in a broad speed distribution of the oxygen. The $\beta$-parameter characterizes as usual the angular distribution for a dipole transition according to $P(\theta) = 1/2(1 + \beta \cdot P_2(\cos(\theta)) \cdot \sin(\theta)$.

In terms of extracting the information about the velocity distribution of the D atoms in the center of mass frame, we have developed a backward reconstruction algorithm based on Bayes' theorem and on a modified Richardson–Lucy algorithm.[66] Here, the problem is not a mere deconvolution because the detection efficiency depends rather strongly on the velocity of the D atoms in the center of mass frame and the kernel function varies with the experimental parameters. This is especially problematic for D atoms significantly faster than the center of mass velocity and scattered into the forward domain. These can be detected in two ways: from the volume behind the detection laser and from the hemisphere behind the dissociation laser, the latter being scattered into the backward domain in the laboratory (see Fig. 1). Thus, the reliability of the forward/backward ratio has to be assessed.

## II. EXPERIMENTAL

The 3D velocity mapping technique has been described in large detail only recently.[67,68] Therefore, the experimental setup will be described only briefly emphasizing the characteristics of the experiment presented here.

The apparatus consists of a homebuilt time of flight (TOF) spectrometer mounted to a commercial 3D imaging detector that consists of a combination of a two stage microchannel plate and a delay line (DL) anode (RoentDek).[69,70]

The TOF spectrometer consists of a repeller plate to which a pulsed nozzle (General Valve, Series 9 Pulsed Valve) is mounted in that way, that the surface of the nozzle flange is within the plane of the electrode surface in order to guarantee a homogeneous field, five ring electrodes comprising the acceleration region of approximately 5 cm (depending on the laser path), a tube of 10 cm length serving as a field free drift region, and two meshes separating the acceleration from the drift region and the drift region from the detector. The spectrometer can be run in two modes: (I) conventional 3D ion imaging, (II) 3D velocity mapping (for details, see Refs. [67] and [68]). The whole setup is housed in a stainless steel vacuum chamber pumped by two turbomolecular pumps (Pfeiffer TMU 260 P, 220 l/s) forepumped by a rotary vane pump filled with perfluoropolyether (PFPE) oil to a background pressure of $10^{-7}$ mbar. When the nozzle is operating, the integral pressure is on the order of $10^{-5}$ mbar.

A mixture of neat D$_2$ and neat N$_2$O with a stagnation pressure of approximately 1 bar or less in order to prevent cluster formation is expanded through the pulsed nozzle (400 $\mu$m orifice). The molecular beam is intersected by two counterpropagating laser beams (ArF Optex 3, Lambda Physik; Nd:YAG pumped Scanmate 2, Coherent) approximately 5 mm downstream of the nozzle orifice and not more than 10 $\mu$s after the rising edge of the gas pulse can be detected in order to keep the gas column between the reaction region and the detector as short as possible, since in this setup the molecular beam is aimed directly at the detector.

The dye laser is focused by an $f=0.3$ m lens into the middle of the molecular beam and is scanned over the deuterium [2+1]-REMPI ($^2$S, 2s $\leftarrow$ $^2$S, 1s) line at 243.067 nm in order to compensate for the Doppler shift. The ArF excimer dissociation laser operating at 193 nm is loosely focused by an $f=0.45$ m CaF$_2$ lens, the focus being approximately 15 cm before the molecular beam, and is polarized by a set of ten CaF$_2$ polarizer plates. The lens is mounted on a combination of two motorized translation stages (Owis, LTM 80) making it possible to position the dissociation laser path very accurately relative to the dye laser.

The pulses coming from the ends of the DL are differentially amplified (KSU EDL DLA800), recorded by a four channel oscilloscope (Waverunner 6050, Quad 5 Gs/s) and fitted by Gaussians in order to obtain the center of the peaks.

## III. DATA ANALYSIS

In reactive collision experiments in which the product is probed by a laser, the problem of biased detection for different velocities arises due to the fact that the volume of the reaction is much larger than the laser focus and the time in which reaction products are built up is long compared to the laser pulse duration. Toomes et al.[8] used the parallel beam technique with a diatomic precursor, Cl$_2$, where the reactant velocity is very well defined. Depending on the delay between the two lasers they showed impressively that almost every kind of product image can be measured. Thus, biased detection is a problem even if the reactant velocity is very well defined and it shows that this is really an inherent problem of state specific laser detection and not of insufficient
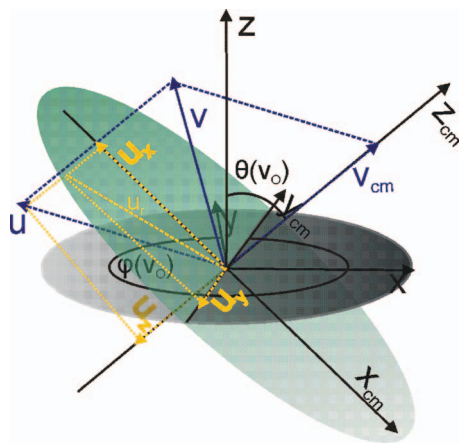
FIG. 2. Illustration of the relevant coordinate systems. The center of mass system which is defined by the velocity of the $O(^1D)$ atom $v_O$ is transformed into the space fixed laboratory coordinate system by rotating it first about the $y_{cm}$ axis by $-\theta(v_O)$ to coincide z and $z_{cm}$ and then by rotating about the common z-axis by $-\varphi(v_O)$. The $y_{cm}$ axis always lies in the laboratory x,y plane (gray). The measured velocity of a D-atom v is shown as the sum of $v_{cm}$ and u. The components of u in the cm system are constructed by projecting (green dotted lines) u first onto $z_{cm}$ ($u_z$) and into the $x_{cm}$, $y_{cm}$ ($u_r$) indicated by the green plane. Finally, $u_r$ is projected onto $x_{cm}$ ($u_x$) and $y_{cm}$ ($u_y$).

reactant preparation. One might think that this destroys the advantage of imaging techniques which is to directly reveal the Newton sphere, but, on the contrary, imaging the product velocity distribution is vital in order to make it possible to unravel the center of mass velocity distribution if the products are to be detected state specifically.

However, in the case of a photoinitiated reaction with laser detection of the product, detected products have to comply with the constraint,

$$(\hat{M}(\theta_{cm}, \varphi_{cm}) \cdot \vec{u} + \vec{v}_{cm})(t_D - t_r) + f_m \vec{v}_{cm} t_r \in V. \tag{1}$$

The rotary matrix $M$ which transforms the velocity of the D atom in the center of mass system $u$ into the laboratory system is given by the initial oxygen velocity vector as is the center of mass velocity $v_{cm}$. The part in the first parenthesis therefore describes the laboratory velocity of the D atom that we will henceforth denote as $v$. By $V$ we mean the volume of the detection laser, $f_m$ denotes the proportionality between the velocity of the oxygen precursor $v_O$ and $v_{cm}$, and $t_D$ and $t_r$ are the delay time and the time of the reaction, respectively. The coordinate systems that will be used are defined as follows: The x-axis of the laboratory system is defined by the dissociation laser, the z-axis coincides with the TOF spectrometer axis, and the y-axis is perpendicular to the x,z-plane. The center of mass system has its z-axis $z_{cm}$ in the direction of the $O(^1D)$ velocity vector and the $u$ vectors are only rotated about the y-axis by the polar angle $\theta(v_O)$ and about the z-axis by the angle $\varphi(v_O)$. This makes $x_{cm}$ and $y_{cm}$ different, but since they have no meaning of their own and we integrate afterwards over the azimuthal angle anyway, we use this convention here for simplicity. The situation is sketched in Fig. 2.

In order to reconstruct the center of mass velocity distribution $P(u)$ from the measured distribution in the laboratory frame $P(v)$, there exist in principle two strategies how to achieve this goal. One is a forward convolution analysis which is common practice but does not yield a unique result, another is a reconstruction based on Bayes theorem, i.e., a calculation on a probabilistic basis to yield the undistorted image which is most likely, given the data and all the information available. Considering the fact that for a formal Bayesian analysis (i.e., the calculation of the posterior mean or the maximum of the posterior distribution) laboratory velocity distributions for all possible center of mass velocity distributions have to be calculated, this seems not a viable solution since the best way to obtain these is a rigorous Monte Carlo simulation.

Another possibility to make an attempt at a probabilistic solution is to start from a deconvolution algorithm derived by Richardson[66] in 1972, that is, based on Bayes' theorem as well. This is an iterative method and shall be presented here in the original representation of Richardson instead of the commonly used form, since it is written in terms of probabilities [Eq. (2)],

$$P_{n+1}(u_i) = \sum_k \frac{P(v_k|u_i)P_n(u_i)}{\sum_j P(v_k|u_j)P_n(u_j)} P(v_k). \tag{2}$$

Here, $u_i$ represents a certain center of mass velocity vector and $v_k$ a certain laboratory velocity vector, i.e., the indices $i$ and $k$ actually represent combinations of three indices each denoting voxels on 3D grids for $(v_x, v_y, v_z)$ and $(u_x, u_y, u_z)$, respectively. The probability $P(v_k|u_i)$ is the conditional probability that a certain velocity vector $v_k$ is measured, if the real center of mass velocity is $u_i$. Thus, this can be identified as the apparatus function which here is a six dimensional tensor. The probability $P(v_k)$ can be identified as the normalized measured image and $P(u_i)$ represents the desired image in the hidden center of mass space. This represents an effective deconvolution algorithm with outstanding robustness with respect to noise and converges rather quickly with growing iteration index $n$ to the undistorted image (for details, of convergence see Refs. 66 and 71–74). As a starting point one can choose a spatially uniform distribution $P_0(u_i)$. However, the problem here is not only a deconvolution from a point spread function [i.e., this would be the spread caused by the spread in $O(^1D)$ velocities] since the detection efficiency for a product with a certain $u_i$ depends on $u$ itself. This is the bias mentioned above. Thus, we need to account for this as well and have done so introducing the detection efficiency tensor $\Phi(u_i)$ so that

$$P(u_i) = \frac{N(u_i)}{\Phi(u_i)}, \tag{3}$$

since we are actually calculating some normalized quantity related to the number $N(u_i)$ of detected products having a center of mass velocity $u_i$ rather than the real distribution $P(u_i)$ if we simply apply Eq. (2) to the normalized product image $P(v_k)$. To see this, we identify the fraction in Eq. (2) by
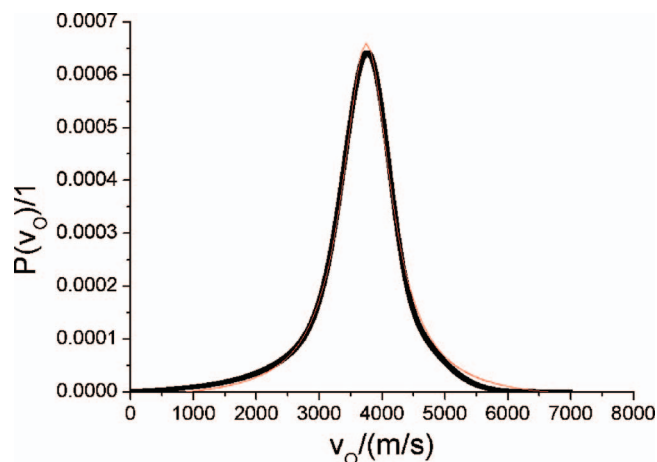
FIG. 3. Speed distribution and least square fit of the O($^1$D) precursor as inferred from Refs. 76 and 77 used in the simulation.

$$P_n(u_i|v_k) = \frac{P(v_k|u_i)P_n(u_i)}{\Sigma_j P(v_k|u_j)P_n(u_j)}. \tag{4}$$

This is really nothing else than Bayes' theorem for the posterior probability $P_n(u_i|v_k)$ in a specific iteration step $n$ which means that here the sum over all $u_i$ must be always 1 because if it is given that a product with $v_k$ has been detected, then it is for sure that it had any velocity in the centre of mass system $u$. Thus, we write instead of Eq. (2),

$$N_{n+1}(u_i) = \sum_k P_n(u_i|v_k)N(v_k), \tag{5}$$

and eventually inserting Eqs. (3) and (4) into Eq. (5) have the result,

$$P_{n+1}(u_i) = \frac{P_n(u_i)}{\Phi(u_i)} \sum_k \frac{P(v_k|u_i)P(v_k)}{\Sigma_j P(v_k|u_j)P_n(u_j)}. \tag{6}$$

Please note that this is a general result because it is not limited to any kind of system. One only has to calculate (or measure if possible) the apparatus function $P(v|u)$ and the detection efficiency $\Phi(u)$.

We did this using a rigorous Monte Carlo method that employs sampling from a spatially uniform $P(u)$ to integrate over the detection time $t_D$ (laser pulse length), the time of the reaction $t_r$ ($0 < t_r < t_D$), the O($^1$D) velocity $v_O$ or equally the center of mass velocity $v_{cm}$, and the dissociation and detection volumes. The latter is in this case a cylinder with the length of the focus volume for a two photon process at the respective wavelength. Simulated products that are at their detection time within this volume are counted as detected. In this we follow Bontuyan *et al.*[75] For the speed distribution of the O($^1$D) precursor we used a model Lorentzian function derived from the results in Ref. 76 and the fit functions provided in Ref. 77 for the photolysis at 205 nm (Fig. 3) and a $\beta$-parameter of 0.49.[76]

Having this result, we can now try to reconstruct simulated distributions for different center of mass velocity distributions. Figures 4(a)–4(c) show plots of three different forward simulated data sets with 10 000 data points. The dye laser is shifted in the $y$-direction by −0.827 mm and in the $z$-direction by 0.1 mm. For the purpose of better orientation, we indicated the direction of the shift on the y-axis by two lines labeled "dissociation" and "detection." The precise values of these in velocity space have no meaning of their own, only the sign of the shift of the detection laser with respect to the dissociation laser is to be made clear. For example, if the detection laser is shifted in the negative $y$-direction this can be also transformed to a negative y-component of a velocity by $\Delta y/t_D$. The delay is 300 ns. In Fig. 4(a) the center of mass velocity distribution $P(u)$ is a spatially uniform distribution and the half length of the focus is 0.5 mm. In Fig. 4(b) the D atoms are scattered only into a narrow solid angle modeled by a $\cos^6(\theta)$ function in the backward hemisphere of the center of mass system; Fig. 4(c) shows the same distribution scattered into the forward hemisphere. Here, the simulated D atoms detected via the two possible paths shown in Fig. 1 are indicated by the respective colors. The ratio of desired and undesired atoms is in this case 6405/3495. In both cases (b and c), the speed distribution is a normal distribution with a mean value of 9000 m/s and a standard deviation of 2800 m/s. The half length of the laser focus is 1.1 mm. Since the length of the focus is moderately crucial for the reconstruction, it has to be estimated within certain bounds. There are two independent ways to do this: (a) the dimensions of the excitation volume for a two-photon process in a Gaussian beam can be calculated from the initial width of the beam and the wavelength; (b) the measured data themselves present an estimate of this length. The latter can be seen in Fig. 4(d) where the forward scattered distribution [Fig. 4(c)] is shown under a different angle. It is not shown here, but the length of the dense part in the middle of Fig. 4(a) is approximately half as long in the direction of the laser beams as in Figs. 4(b) and 4(c). Thus, comparison of measured data (see Sec. V) with simulations together with strategy (a) leads us to the conclusion that the half length of the focus is between 0.5 and 1.1mm, i.e., $0.8 \pm 0.3$ mm. We will include this in the estimation of errors in the results. Figure 4(d) also shows that detection by 3D velocity mapping is the method of choice for these experiments, since (i) the cylindrical symmetry of the laboratory velocity distribution is lost and (ii) normal 3D ion imaging would impose an additional convolution with the length of the focus of the dissociation laser on the measured distribution. Upon further inspection of Fig. 4 it is clear that the reconstruction will have to cope with the problem of reproducing the correct forward/backward ratio, since the forward scattered products [Figs. 4(c) and 4(d)] are also scattered into the domain of the backward scattered products (see also Fig. 1). Furthermore, the detection efficiency for the forward scattered products is higher. However, it turns out that these pure cases are already the most crucial, since the error made by the reconstruction cancels partly out in "mixed" distributions so that less iterations are necessary to reconstruct these (*vide infra*).

Figure 5 shows the results for the reconstruction of the simulated distributions from Fig. 4. For the representation of the data we chose a meridian plot[78] which is not equal to, but conveys the same information as the double DCS. Briefly, it is obtained by projecting each point into a certain plane leaving the distance to the origin and the angle in this plane constant. Figures 5(a)–5(c) show the problematic reconstruc-
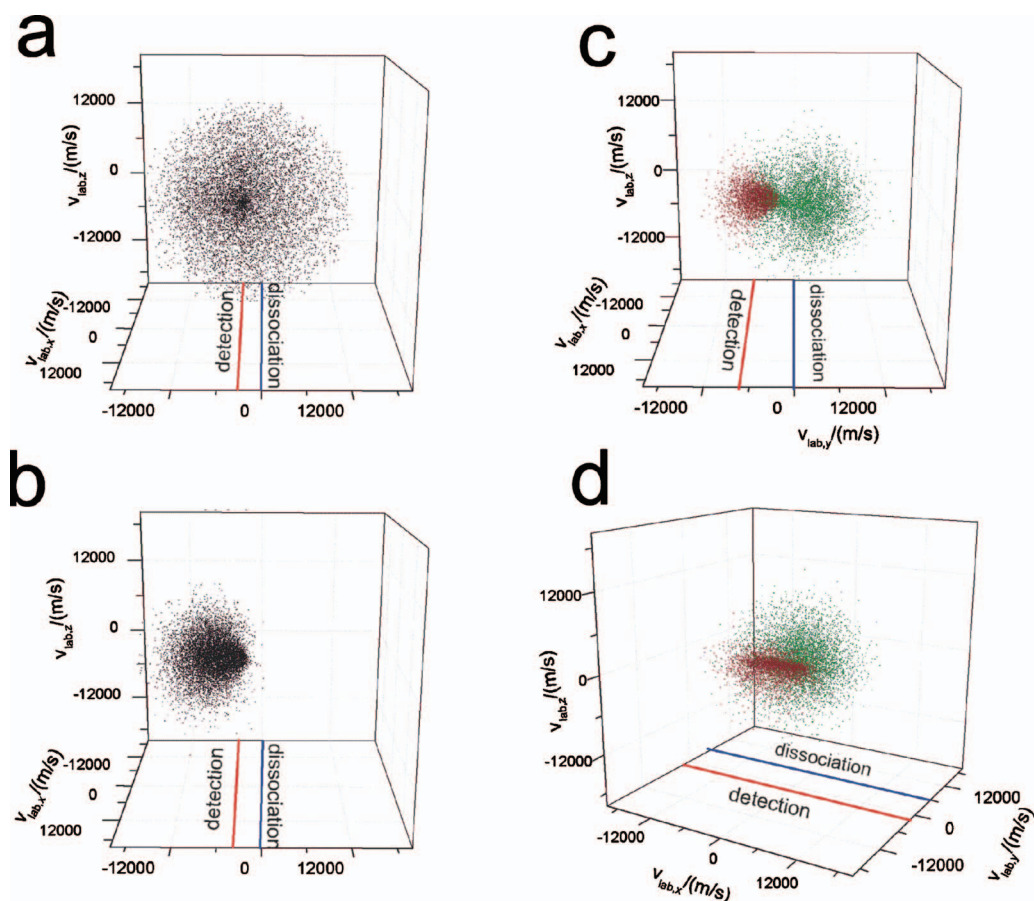
FIG. 4. Forward simulated laboratory velocity distributions of D atoms for different center of mass velocity distributions. (a) Spatially uniform distribution with $v_{max} = 16000$ m/s. (b) Backward scattering, normal speed distribution with mean of 9000 m/s and $\sigma = 2800$ m/s. (c) Forward scattering, speed distribution as in (b). The ions detected on the two possible paths shown in Fig. 1 are represented by the respective color. Their numbers are olive (desired): 6405; wine (unwanted): 3595. (d) The same point cloud as in (c) but from a different angle. The lines labeled with dissociation and detection shall serve as a help for orientation only. The exact velocity values associated with them have no meaning of their own.

tion of D atoms solely backscattered after an increasing number of iterations. As one might guess, the algorithm initially assigns the most part of the probability density to the forward scattered products, since the detection efficiencies for these are higher. But, as the iteration index grows, the lack of products in the domain that can be assigned unambiguously to forward scattering leads to a gradual decrease in the forward direction. Figure 5(d) shows the reconstruction of forward scattered products after 60 iterations. As this was initially thought to be the most problematic case to tell apart from a forward-backward symmetric distribution, the result seems very satisfying. Figure 5(e) shows the reconstruction of the spatially uniform distribution shown in Fig. 4(a) after 150 iterations. Figures 6 and 7 show the DCSs and the speed distributions for the simulated product clouds in Fig. 4(a) (Fig. 6) and Fig. 4(c) (Fig. 7). On the left hand side we show the distributions before reconstruction and on the right hand side after reconstruction [i.e., these represent Figs. 5(e) and 5(d) integrated over the angle and the radius, respectively]. The red dashed curves represent the functions as implemented in the respective simulations. The left hand side of Fig. 6 shows the phenomenon that the angular bias is canceled out for an isotropic distribution $P(u)$, but the speed distribution remains biased. Figure 7 shows how well the broadening resulting from the reactant velocity spread is ac-

tually removed. The Gaussian fit (blue, dashed dotted) has a mean value of $9221 \pm 74$ m/s and a standard deviation of $2838 \pm 82$ m/s, being almost ideally the same as the original values 9000 and 2800 m/s, respectively. Regarding this, it seems strange that the falling edge in Fig. 6 is not so well reproduced. Presumably this is because the probability density is transferred from small to large velocities during the reconstruction. However, the reconstructed DCS in Fig. 7 fits nicely to the ideal function at the pole with a small "background" remaining which is isotropically distributed.

## IV. CALIBRATION OF THE SPATIAL LASER SHIFT

From the description of the data analysis in Sec. III it is clear that we have to be able to measure the spatial shift between the dissociation and detection laser beams in order to be able to interpret the product velocity distribution of the reaction of $O(^1D)$ with $D_2$. Therefore, a method to measure this distance as accurately as possible must be devised. We have chosen to use the following procedure.

(i)    HBr is photolyzed both at the REMPI detection wavelength for hydrogen (243 nm) and at the wavelength of the ArF-excimer laser (193 nm) shifted to some distance by the step motors of the stages on which the focusing lens is mounted.
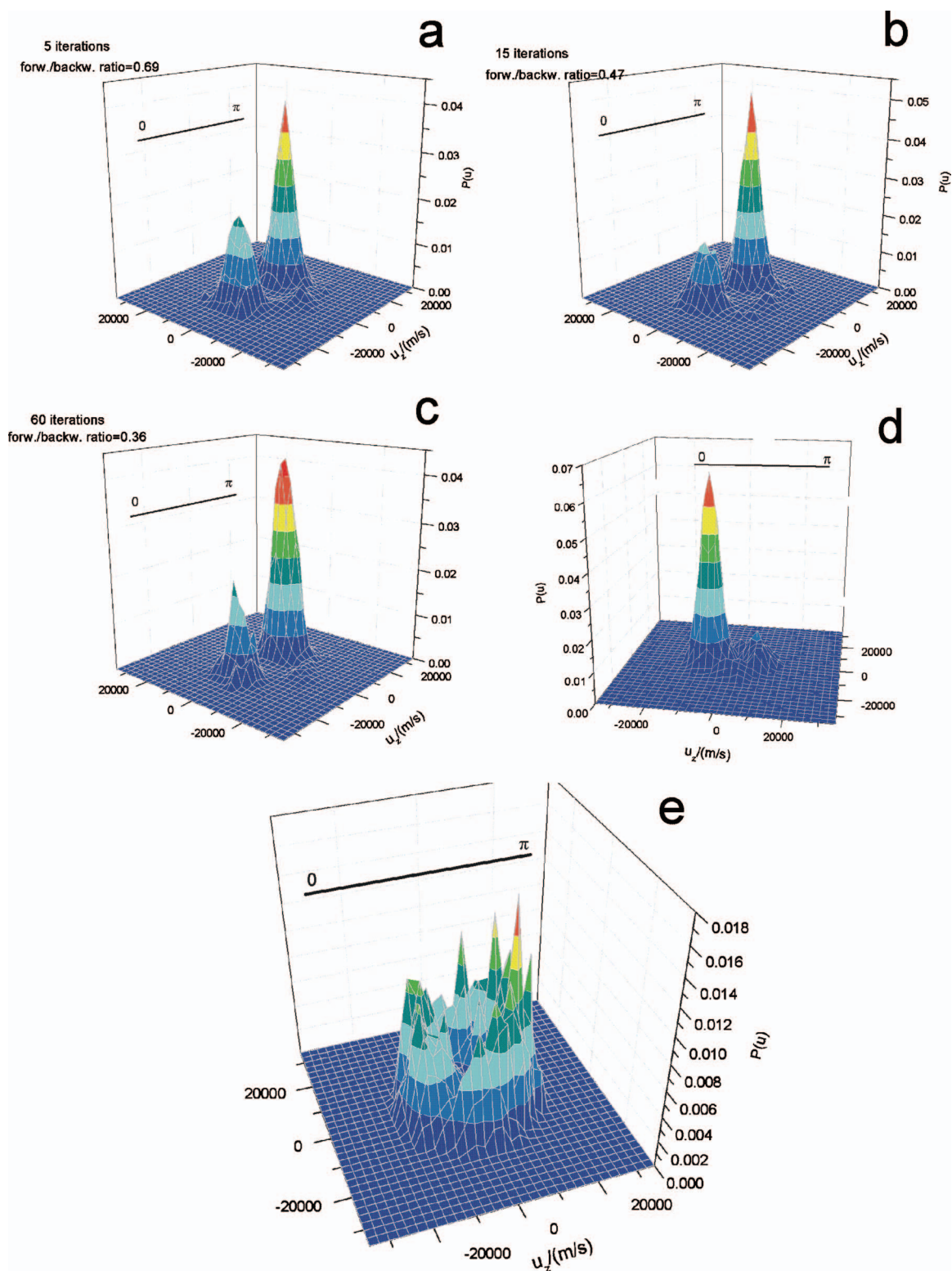
FIG. 5. Reconstruction of the simulated data in Fig. 4. [(a)–(c)] Backward scattered D atoms for different iteration index. (d) Forward scattered D atoms for 150 iterations. (e) Spatially uniform D atom velocity distribution

(ii)     The H atoms produced in both laser beams are ionized by [2+1] REMPI only inside the dye laser focus.

(iii)    The velocities of this composed H$^+$ ion distribution are mapped three dimensionally (see Fig. 8). Additionally, the dye laser is operated at a fixed wavelength. Thus, only a Doppler selected slice of the real distribution is mapped which increases the resolution of the calibration procedure.

(iv)    As Fig. 8 shows, the measured distribution consists of two parts: a Doppler slice of two rings with opposite anisotropies belonging to the 243 nm photodissociation and two spots outside these rings belonging to the faster H atoms from the 193 nm dissociation that have been scattered into the appropriate solid angle to be inside the dye laser focus at the time that it fires. Note that there are two parts for each wavelength due to the
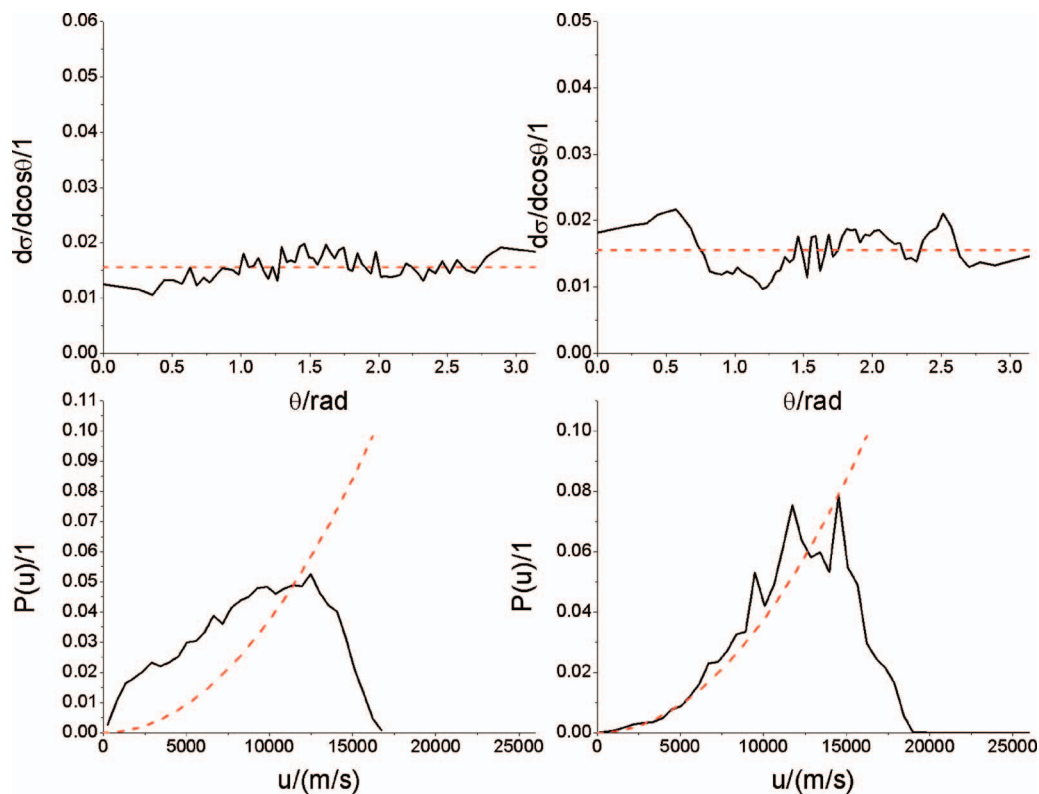
FIG. 6. Comparison of the DCSs and speed distributions (black, solid) of the simulated distribution in Fig. 4(a) before (left) and after (right) the reconstruction with the ideal functions used in the simulation (red, dashed). One clearly sees that the bias in the speed distribution has been removed successfully and the bias in the DCS was not very large before the reconstruction anyway. This is due to the fact that the biases from forward and backward scattered products cancel each other out. Note that the noise magnification is quite low, too.
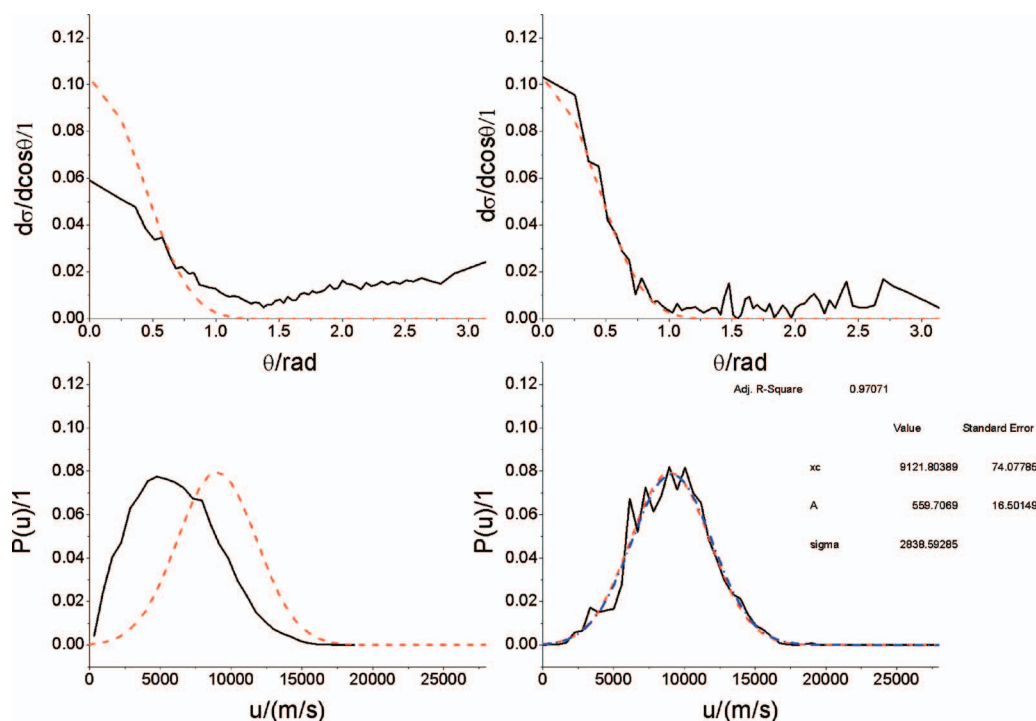


FIG. 7. Comparison of the DCSs and speed distributions (black, solid) of the simulated distribution in Fig. 4(c) before (left) and after (right) the reconstruction with the ideal functions used in the simulation (red, dashed). The bias has been removed successfully from both the angular and the speed distribution. The Gaussian fit (blue, dash-dotted) gives a hint of the remaining broadening due to the spread in reactant velocities (see text).
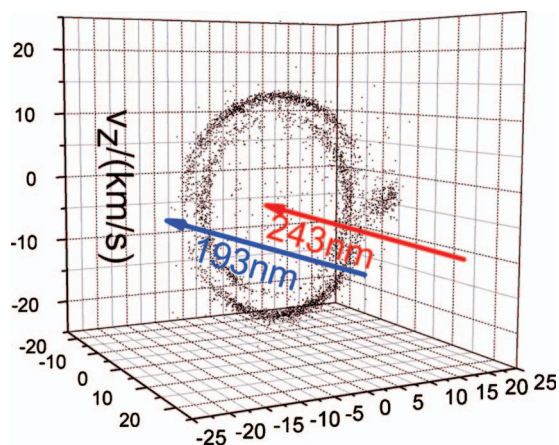
FIG. 8. Doppler sliced 3D velocity map of H atoms emerging from the photodissociation of HBr at 243 nm [two rings with opposite $\beta$ for the Br($^2$P$_{1/2}$) and the Br($^2$P$_{3/2}$) channel, respectively] and 193 nm shifted perpendicular to the z-axis (dots on the right hand side of the outer ring). The H atoms are detected by REMPI[2+1] at 243 nm. The arrows labeled with the dissociation and detection wavelengths shall serve as a help for orientation only. The exact velocity values associated with them have no meaning of their own.

two spin orbit states of the bromine partner fragment, i.e., Br($^2$P$_{3/2}$) and Br($^2$P$_{1/2}$), respectively.[79]

(v)    From the measured velocity of the two spots belonging to the 193 nm dissociation one can calculate the distance between the two lasers using the simple relation $\Delta s = v \cdot t_D$. Note that the presence of the 243 nm rings actually helps a lot in finding the zero velocity due to their symmetry.

However, the Doppler slice of the H atom distribution is not infinitely thin, the speed distribution for each ring is not a delta function due to the spectral width of the excimer laser, and the starting point of the H atom trajectories is blurred by the radius of the same laser. Therefore, the focusing lens is scanned in order to find the point of maximum intensity for each of the two 193 nm spots. The same procedure can be repeated on the opposite side of the detection laser for the y-direction and for the two respective positions in the z-direction. Thus, we end up with four values (two "spots" on each of the opposite sides of the detection laser) for the distance $\Delta s$ for each of the two dimensions orthogonal to the laser beam propagation, i.e., y and z, as a function of the step motor position of the stages on which the focusing lens is mounted. A linear regression with setting the intercept to zero yields the slopes,

$$\Delta y_{laser}/\Delta y_{lens} = 103.5 \pm 0.8 \ [\mu m/1000 \text{ steps}], \qquad (7)$$

$$\Delta z_{laser}/\Delta z_{lens} = 25.0 \pm 0.2 \ [\mu m/1000 \text{ steps}]. \qquad (8)$$

A simple estimate to validate this result can be made by using the specifications of the manufacturer for the motorized stages (Owis, LTM 80): 78.1 $[\mu m/1000$ steps] for the linear stage in the y-direction and a ratio $\Delta y/\Delta z = 4$. Since the 45 cm lens is moved approximately 15 cm out of focus, this would yield $\Delta y_{laser}/\Delta y_{lens} = 104.1$ $[\mu m/1000$ steps] and $\Delta z_{laser}/\Delta z_{lens} = 26.0$ $[\mu m/1000$ steps], respectively.
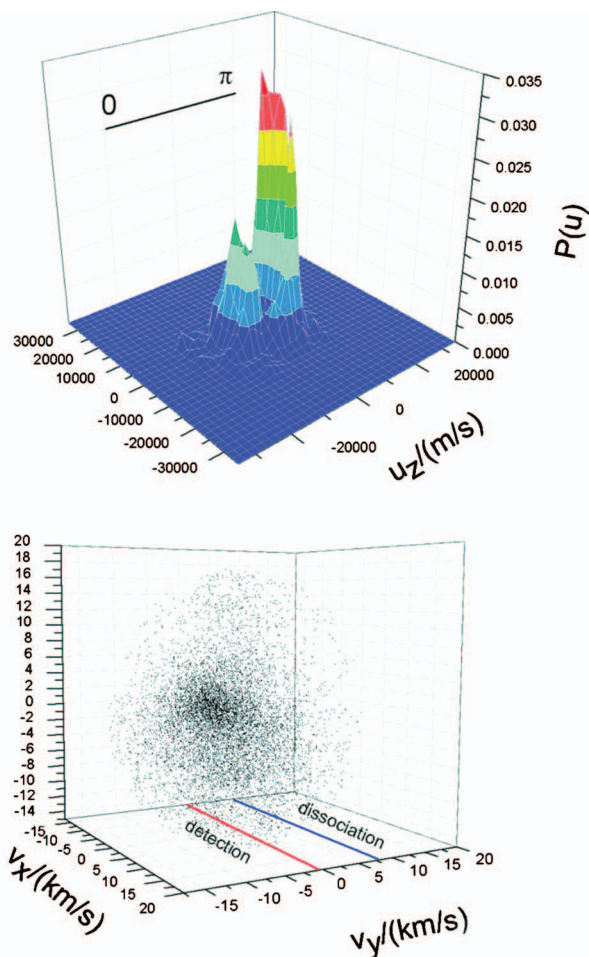


FIG. 9. Raw data of D atom laboratory velocities and meridian plot of the reconstructed center of mass velocity distribution after background correction. The lines labeled with dissociation and detection in the lower panel shall serve as a help for orientation only. The exact velocity values associated with them have no meaning of their own.

## V. RESULTS: D ATOM PRODUCT VELOCITY DISTRIBUTION

We have measured the D atom velocity distribution emerging from the reaction of O($^1$D) with D$_2$ by photolyzing N$_2$O molecules at 193 nm as precursors for O($^1$D) atoms in a molecular beam of a 1:1 mixture of neat N$_2$O with D$_2$. The D atoms were ionized by [2+1] REMPI at 243 nm with the detection laser shifted by $\Delta y = -967 \pm 15$ $\mu m$ with respect to the dissociation laser, i.e., as in the simulations in Sec. III in the negative y-direction. The delay was $t_D = 300$ ns. We estimated the error for the laser shift to be approximately two standard deviations obtained for the calibration in Sec. IV due to the additional uncertainty in finding the zero overlap. The results are shown in Figs. 9 and 10. The 3D velocity distribution of the raw data shown in the lower panel of Fig. 9 yields the reconstructed image presented as a meridian plot in the upper panel. The accumulation of ions at negative $v_z$ is due to background from a heavier mass which has been removed in the reconstructed center of mass distribution. The error bars in Fig. 10 have been obtained by reconstructing the image also for detection laser focus half lengths of $l_{det} = 0.8 \pm 0.3$ mm and laser shifts of $\Delta y = -967 \pm 15$ $\mu m$. The
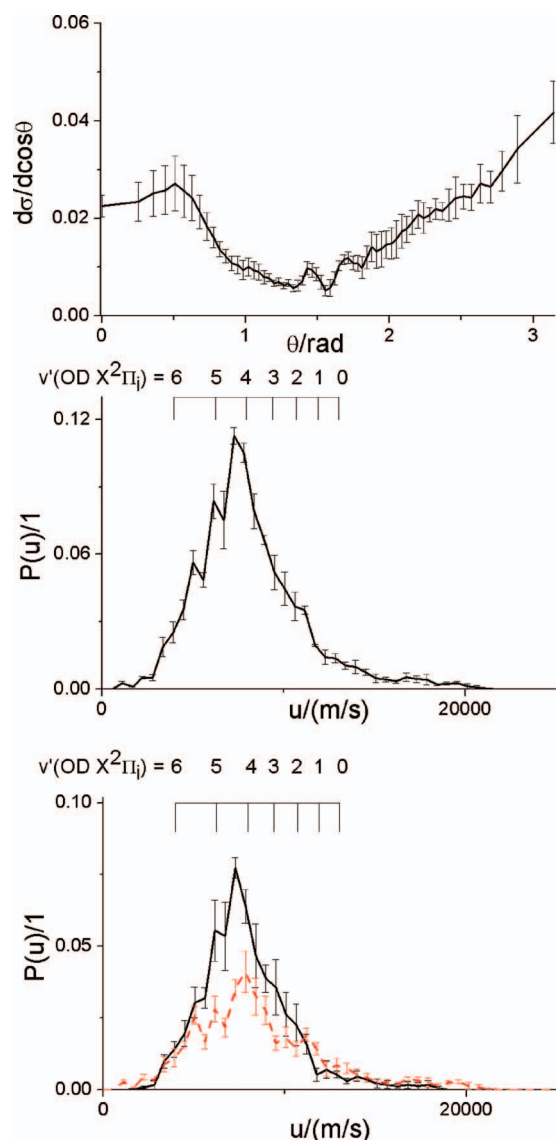
FIG. 10. Upper panel: DCS of the D-atoms emerging from the reaction of $O(^1D)+D_2$; middle panel: speed distribution; lower panel: speed distribution decomposed into forward and backward scattering (black/solid: backward hemisphere; red/dashed: forward hemisphere).



FIG. 11. Collision energy distribution and O atom precursor velocity distribution from a Monte Carlo simulation assuming a Gaussian center of mass speed distribution of D atoms with 9000 m/s as the center and a standard deviation of 2800 m/s using the experimental parameters $t_D=300$ ns and $\Delta y=-967$ $\mu$m. The lines labeled with dissociation and detection in the lower panel shall serve as a help for orientation only. The exact velocity values associated with them have no meaning of their own.

results have been averaged to yield the speed and angular distributions. The error bars are therefore the mean quadratic deviation from the mean values.

The meridian plot in Fig. 9 shows that the D atoms are scattered predominantly into the backward direction. The backward distribution is broader than the forward peak, which has been termed an "arrowhead" shape by Ahmed *et al.*[56] The backward scattering is more pronounced than in their study but the collision energy is also considerably larger ($5.2 \pm 1.9$ kcal/mol, see Fig. 11). Considering this, it is in accord with the interpretation that the collinear abstraction mechanism via excited PESs is becoming more important compared to the insertion via a $D_2O$ intermediate over the ground PES $1\ ^1A'$ as the collision energy increases. The lowest excited PES, $1\ ^1A''$, shows a barrier for collinear approach of approximately 2.4 kcal/mol.[51]

The measured center of mass speed distributions of D atoms in the forward and backward domains are shown in

Fig. 10 together with the allowed speeds for the vibrational states of the OD partner fragment and the DCS.[77] It shows that $v'=4,5$ are the most populated vibrational levels (energies derived from Ref. 80) and that the extra atoms scattered in the backward direction are in the high vibrational states in accord with previous findings by Liu *et al.*[57] who compared the collision energies of 2.0 and 3.2 kcal/mol and reported that the extra D atoms scattered in the backward direction are formed with the OD in the vibrational states $v'=4-6$. The backward peak in Fig. 9 is at approximately 7000 m/s which is just between $v'=4$ and 5. According to Aoiz and coworkers[81,82] who calculated the DCSs for HD at the collision energies used in the study of Liu *et al.*[57] on the $(1\ ^1A')$, $(1\ ^1A'')$, and the $(2\ ^1A')$ surface, the backward preference is also present on the ground PES for the higher collision energy (138.8 meV/3.2 kcal/mol). Additionally, the 7% contribution from the $(1\ ^1A'')$ surface is exclusively backward scattered and the 3% that proceed nonadiabatically via the $(2\ ^1A')$ and reach the ground state products through a conical intersection are also predominantly backward scattered.

This would yield a forward/backward ratio of less than 0.8. Considering that our mean collision energy is $5.22 \pm 1.9$ kcal/mol, the forward backward ratio of 0.7 seems reasonable. Comparing the shape of our DCS with that in Ref. 54 where the D product distribution for the reaction of O($^1$D) with HD at 4.53 kcal/mol was measured with our relative DCS, it has the same ratio on the poles and also the overall shape seems similar as well.

Note the simulated spatial velocity distribution of O($^1$D) atoms that have been the precursor of an actually detected reaction product assuming the Gaussian speed distribution used in Figs. 4(b)–4(d) and a spatially isotropic angular distribution (Fig. 11). This shows that the precursor velocity has indeed been selected according to the direction in which the lasers have been shifted. The $v_{O,y}$ distribution peaks at approximately 3200 m/s which is very close to the value 3233 m/s that can be inferred from the ratio of the laser shift and the time delay. The spread in the collision energy could be avoided by using a diatomic precursor molecule if this presented a viable solution for the reaction to be studied. However, it has been shown that the DCS can nevertheless be extracted from the data also if no appropriate diatomic precursor can be used.

## VI. CONCLUSION

In this contribution we presented a method to measure the quantum state selective DCS of photoinitiated reactive collisions that combines features of the PHOTOLOC[1–23] and the parallel molecular beams technique[7–9] using REMPI detection in a single molecular beam. Under the conditions of PHOTOLOC (high reactant densities), we were able to select reactant velocities from a small solid angle by shifting the dissociation and detection lasers in time and space which leads to a better definition of the center of mass velocity. Like in the case of parallel beams,[8] the conditions (detection volume much smaller than the reaction volume, time span for the reaction much longer than the laser pulse length) give rise to biased detection of the reaction products. We have devised an algorithm that removes this bias and additionally deconvolutes the product distribution from the apparatus function. This makes it possible to use also precursor molecules that produce a large spread of reactant kinetic energies upon photolysis if experimental necessities should demand it (e.g., if more complex reactants are to be generated by photolysis). In this case, knowledge of the precise collision energy is of course sacrificed. We have shown the applicability of the technique using the benchmark reaction O($^1$D)+D$_2$ with N$_2$O as the precursor for the O($^1$D)-atom and detecting the D atom by REMPI[2+1] at 243 nm. Since the D atoms are much quicker than the oxygen reactants and the product kinetic energy distribution is very broad, this reaction could not be treated by PHOTOLOC. However, we managed to obtain the DCS in agreement with previous studies using our new technique and we were able to add more evidence to the idea that at high collision energies (i.e., $5.2 \pm 1.9$ kcal/mol) a collinear abstraction mechanism leads to backward scattering with the OD predominantly in the vibrational states $v'$ =4 and 5 in addition to an insertion mechanism on the

ground PES. This is the only reaction path below 2.4 kcal/mol collision energy corresponding to the lowest barrier for a collinear approach.[51]

Since the resulting laboratory velocity distribution is not cylindrically symmetric, 3D velocity mapping is the method of choice for these measurements.

The reconstruction is rather sensitive to the correct distance between the lasers and to a lower extent to the length of the detection volume. We have shown here a simple method by which we can measure this distance with an accuracy of approximately 1%, becoming approximately 2% if one considers the problem of finding the zero overlap of the two beams. Furthermore, it is convenient that the data themselves give a good estimate of the length of the laser focus by the dimensions of the product velocity distribution in the direction of the laser beam propagation.

## ACKNOWLEDGMENTS

[1] N. E. Shafer, A. J. Orr-Ewing, W. R. Simpson, H. Xu, and R. N. Zare, Chem. Phys. Lett. **212**, 155 (1993).

[2] F. J. Aoiz, M. Brouard, P. A. Enriquez, and R. Sayos, J. Chem. Soc., Faraday Trans. **89**, 1427 (1993).

[3] N. E. Shafer-Ray, A. J. Orr-Ewing, and R. N. Zare, J. Phys. Chem. **99**, 7591 (1995).

[4] M. J. Bass, M. Brouard, C. Vallance, T. N. Kitsopoulos, P. C. Samartzis, and R. L. Toomes, J. Chem. Phys. **119**, 7168 (2003).

[5] M. J. Bass, M. Brouard, C. Vallance, T. N. Kitsopoulos, P. C. Samartzis, and R. L. Toomes, J. Chem. Phys. **121**, 7175 (2004).

[6] M. J. Bass, M. Brouard, R. Cireasa, A. P. Clark, and C. J. Vallance, Chem. Phys. **123**, 094301 (2005).

[7] X. Liu, R. L. Gross, and A. G. Suits, J. Chem. Phys. **116**, 5341 (2002).

[8] R. L. Toomes and T. N. Kitsopoulos, Phys. Chem. Chem. Phys. **5**, 2481 (2003).

[9] C. Murray, A. J. Orr-Ewing, R. L. Toomes, and T. N. Kitsopoulos, J. Chem. Phys. **120**, 2230 (2004).

[10] A. C. Luntz, R. Schinke, W. A. Lester, Jr., and H. H. J. Günthard, Chem. Phys. **70**, 5908 (1979).

[11] R. J. Buss, P. Casavecchia, T. Hirooka, S. J. Sibener, and Y. T. Lee, Chem. Phys. Lett. **82**, 386 (1981).

[12] P. A. Whitlock, J. T. Muckerman, and E. R. J. Fisher, Chem. Phys. **76**, 4468 (1982).

[13] R. Polák, I. Paiderová, and P. J. Kuntz, J. Chem. Phys. **87**, 2863 (1987).

[14] P. J. Kuntz, B. I. Niefer, and J. J. Sloan, J. Chem. Phys. **88**, 3629 (1988).

[15] P. J. Kuntz, B. I. Niefer, and J. J. Sloan, J. Chem. Phys. **151**, 77 (1991).

[16] S. P. Walch and L. B. Harding, J. Chem. Phys. **88**, 7653 (1988).

[17] P. Casavecchia, N. Balucani, M. Alagia, L. Cartechini, and G.G. Volpi, Acc. Chem. Res. **32**, 503 (1999).

[18] X. Liu, J. J. Lin, S. Harich, and X. Yang, J. Chem. Phys. **113**, 1325 (2000).

[19] X. Liu, J. J. Lin, S. Harich, G. C. Schatz, and X. Yang, Science **289**, 1536 (2000).

[20] X. Liu, C. C. Wang, S. A. Harich, and X. Yang, Phys. Rev. Lett. **89**, 133201 (2002).

[21] K. Yuan, Y. Cheng, X. Liu, S. A. Harich, X. Yang, and D.-H. Zhang, Phys. Rev. Lett. **96**, 103202 (2006).

[22] F. J. Aoiz, L. Bañares, J. F. Castillo, V. J. Herrero, B. Martinez-Haya, P. Honvault, J. M. Launay, X. Liu, J. J. Lin, S. A. Harich, C. C. Wang, and X. Yang, J. Chem. Phys. **116**, 10692 (2002).

[23] M. H. Alexander, E. J. Rackham, and D. E. Manolopoulos, J. Chem. Phys. **121**, 5221 (2004).

[24] F. J. Aoiz, L. Bañares, J. F. Castillo, B. Martinez-Haya, and M. P. Miranda, J. Chem. Phys. **114**, 8328 (2001).

[25] N. Balucani, P. Casavecchia, F. J. Aoiz, L. Bañares, J. F. Castillo, and V. J. Herrero, Mol. Phys. **103**, 1703 (2005).

[26] F. J. Aoiz, L. Bañares, and V. J. Herrero, J. Phys. Chem. A **110**, 12546 (2006).

[27] G. K. Smith and J. E. Butler, J. Chem. Phys. **73**, 2243 (1980).

[28] G. M. Jursich and J. R. Wiesenfeld, Chem. Phys. Lett. **119**, 511 (1985).

[29] J. E. Butler, G. M. Jurisch, I. A. Watson, and J. R. Wiesenfeld, J. Chem. Phys. **84**, 5365 (1986).

[30] C. B. Cleveland, G. M. Jurisch, M. Trolier, and J. R. Wiesenfeld, J. Chem. Phys. **86**, 3253 (1987).

[31] K. Mikulecky and K.-H. Gericke, J. Chem. Phys. **96**, 7490 (1992).

[32] K. Mikulecky and K.-H. Gericke, Chem. Phys. **175**, 13 (1993).

[33] Y. Huang, Y. Gu, C. Liu, X. Yang, and Y. Tao, Chem. Phys. Lett. **127**, 432 (1986).

[34] J. E. Butler, R. G. Mac Donald, D. J. Donaldson, and J. J. Sloan, Chem. Phys. Lett. **95**, 183 (1983).

[35] P. M. Aker and J. J. Sloan, J. Chem. Phys. **85**, 1412 (1986).

[36] L. Holmlid and K. Rynefors, Chem. Phys. **60**, 393 (1981).

[37] K. Rynefors and L. Holmlid, Chem. Phys. **60**, 405 (1981).

[38] K. Rynefors, P.-A. Elofson, and L. Holmlid, Chem. Phys. **100**, 53 (1985).

[39] P.-A. Elofson, K. Rynefors, and L. Holmlid, Chem. Phys. **100**, 39 (1985).

[40] F. J. Aoiz, L. Bañares, J. F. Castillo, M. Brouard, W. Denzer, C. Vallance, P. Honvault, J.-M. Launay, A. J. Dobbyn, and P. J. Knowles, Phys. Rev. Lett. **86**, 1729 (2001).

[41] E. J. Rackham, F. Huarte-Larrañaga, and D. E. Manolopoulos, Chem. Phys. Lett. **343**, 356 (2001).

[42] K. Drukker and G. C. Schatz, J. Chem. Phys. **111**, 2451 (1999).

[43] S. K. Gray, C. Petrongolo, K. Drukker, and G. C. Schatz, J. Phys. Chem. A **103**, 9448 (1999).

[44] F. J. Aoiz, T. González-Lezana, and V. Sáez Rábanos, J. Chem. Phys. **129**, 094305 (2008).

[45] R. Schinke and W. A. Lester, Jr., J. Chem. Phys. **72**, 3754 (1980).

[46] A. J. Alexander, F. J. Aoiz, M. Brouard, I. Burak, Y. Fujimura, J. Short, and J. P. Simons, Chem. Phys. Lett. **262**, 589 (1996).

[47] A. J. Alexander, F. J. Aoiz, M. Brouard, and J. P. Simons, Chem. Phys. Lett. **256**, 561 (1996).

[48] A. J. Alexander, D. A. Blunt, M. Brouard, J. P. Simons, F. J. Aoiz, L. Bañares, Y. Fujimura, and M. Tsubouchi, Faraday Discuss. **108**, 375 (1997).

[49] A. J. Alexander, F. J. Aoiz, L. Bañares, M. Brouard, J. Short, and J. P. Simons, J. Phys. Chem. A **101**, 7544 (1997).

[50] Y.-T. Hsu, J.-H. Wang, and K. Liu, J. Chem. Phys. **107**, 2351 (1997).

[51] G. C. Schatz, L. A. Pederson, and P. J. Kuntz, Faraday Discuss. **108**, 357 (1997).

[52] G. C. Schatz, A. Papaioannou, L. A. Pederson, L. B. Harding, T. Hollebeek, T.-S. Ho, and H. Rabitz, J. Chem. Phys. **107**, 2340 (1997).

[53] Y.-T. Hsu and K. Liu, J. Chem. Phys. **107**, 1664 (1997).

[54] D.-C. Che and K. Liu, J. Chem. Phys. **103**, 5164 (1995).

[55] N. Alagia, N. Balucani, L. Cartechini, P. Casavecchia, E. H. van Kleef, G. G. Volpi, P. J. Kuntz, and J. J. Sloan, J. Chem. Phys. **108**, 6698 (1998).

[56] M. Ahmed, D. S. Peterka, and A. G. Suits, Chem. Phys. Lett. **301**, 372 (1999).

[57] X. Liu, J. J. Lin, S. A. Harich, and X. Yang, Phys. Rev. Lett. **86**, 408 (2001).

[58] P. Casavecchia, Rep. Prog. Phys. **63**, 355 (2000).

[59] T.-Y. Chen, W.-P. Zhang, X.-Q. Wang, and G.-J. Zhao, Chem. Phys. **365**, 158 (2009).

[60] C.-Y. Hou, Y.-M. Li, and D.-Zhao, Chem. Phys. **364**, 64 (2009).

[61] G. S. Selwyn and H. S. Johnston, J. Chem. Phys. **74**, 3791 (1981).

[62] T. F. Hanisco and A. C. Kummel, J. Phys. Chem. **97**, 7242 (1993).

[63] R. Simonaitis, R. I. Greenberg, and J. Heicklen, Int. J. Chem. Kinet. **4**, 197 (1972).

[64] P. Felder, B. M. Haas, and R. J. Huber, Phys. Chem. Lett. **186**, 177 (1991).

[65] T. Nakayama, K. Takahashi, Y. Matsumi, N. Taniguchi, and S. Hayashida, J. Geophys. Res. **108**, 4668 (2003).

[66] W. H. Richardson, J. Opt. Soc. Am. **62**, 55 (1972).

[67] S. Kauczok, N. Gödecke, A. I. Chichinin, M. Veckenstedt, C. Maul, and K.-H. Gericke, Rev. Sci. Instrum. **80**, 083301 (2009).

[68] A. I. Chichinin, S. Kauczok, K.-H. Gericke, and C. Maul, Int. Rev. Phys. Chem. **28**, 607 (2009).

[69] O. Jagutzki, V. Mergel, K. Ullmann-Pfleger, L. Spielberger, U. Spillmann, R. Dorner, and H. Schmidt-Böcking, Nucl. Instrum. Methods Phys. Res. A **477**, 244 (2002).

[70] I. Ali, R. Dörner, O. Jagutzki, S. Nüttgens, V. Mergel, L. Spielberger, K. Khayyat, T. Vogt, and H. Bräuning, Nucl. Instrum. Methods Phys. Res. B **149**, 490 (1999).

[71] T. J. Kennett, W. V. Prestwich, and A. Robertson, Nucl. Instrum. Methods **151**, 285 (1978).

[72] T. J. Kennett, W. V. Prestwich, and A. Robertson, Nucl. Instrum. Methods **151**, 293 (1978).

[73] T. J. Kennett, P. M. Brewster, W. V. Prestwich, and A. Robertson, Nucl. Instrum. Methods **153**, 125 (1978).

[74] L. B. Lucy, Astron. J. **79**, 745 (1974).

[75] L. S. Bontuyan, A. G. Suits, P. L. Houston, and B. J. Whitaker, J. Phys. Chem. **97**, 6342 (1993).

[76] M. Ahmed, E. R. Wouters, D. S. Peterka, O. S. Vasyutinskii, and A. Suits, Faraday Discuss. **113**, 425 (1999).

[77] T. Suzuki, H. Katayanahi, Y. Mo, and K. Tonokura, Chem. Phys. Lett. **256**, 90 (1996).

[78] A. I. Chichinin, T. Einfeld, C. Maul, and K.-H. Gericke, Rev. Sci. Instrum. **73**, 1856 (2002).

[79] T. P. Rakitzis, P. C. Samartzis, R. L. Toomes, and T. N. Kitsopoulos, J. Chem. Phys. **121**, 7222 (2004).

[80] K. P. Huber and G. Herzberg, *Constants of Diatomic Molecules* (Van Nostrand Reinhold, New York, 1979).

[81] F. J. Aoiz, L. Bañares, J. F. Castillo, V. J. Herrero, and B. M. Martinez-Haya, Phys. Chem. Chem. Phys. **4**, 4379 (2002).

[82] F. J. Aoiz, L. Bañares, M. Brouard, J. F. Castillo, and V. J. Herrero, J. Chem. Phys. **113**, 5339 (2000).